Wideband, Compact Antennas with Interdigitated Magnetic-based Near-field Resonant Parasitic Elements

Xiaoming Chen, Ming-Chun Tang, Da Yi, and Richard W. Ziolkowski

***Abstract* —Wideband, compact antennas based on interdigitated magnetic-based near-field resonant parasitic (NFRP) elements are presented. The interdigitated NFRP elements, driven with coax-fed monopole antennas, facilitate the realization of two adjacent resonant modes whose combination yields the enhanced bandwidth. The resulting wideband compact antennas exhibit broadside radiation performance. Linearly polarized (LP) and circularly polarized (CP) prototypes based on this interdigitated NFRP element concept were designed, simulated, fabricated, and measured. The measured and simulated results are in good agreement. The NFRP radiating element of the LP antenna is electrically small with $ka = 0.921$ and yields a wide, 17.4%, –10-dB impedance bandwidth with a stable realized gain, ~ 5.5 dBi, over its entire operational bandwidth. The NFRP radiating element of the CP antenna is also electrically small with $ka = 0.923$ and exhibits a wide, 8.6%, 3-dB axial ratio bandwidth. Stable realized gain, ~5.2 dBi, and uniform radiation patterns along with relatively high radiation efficiency, $RE > 88\%$, are achieved over its entire operational bandwidth.**

***Index Terms* —Bandwidth, compact antennas, interdigitated structures, linear and circular polarization, magnetic-based near-field resonant parasitic (NFRP) elements, NFRP antennas.**

I. Introduction

Resonant magnetic-based antennas have advanced near-field and mid-range wireless power transfer applications [1]. Similarly, electrically small antennas (ESAs), i.e., antennas that satisfy $ka < 1$, where $k = 2\pi/\lambda_0 = 2\pi f_0/c$, λ_0 being the free-space wavelength corresponding to the operating frequency f_0 and a is the radius of the smallest sphere that completely encloses the entire antenna system [2], with magnetic-based near-field resonant parasitic (NFRP) elements [3], [4] have been applied in many space-limited platforms. These include wearable applications [5], mobile ionospheric heaters [6], and wireless power transfer [7]. However, the minimum quality factor for a magnetic ESA is a factor two larger than an electric one with same electric size: $Q_{mag} = 2\,Q_{elec} = 3\,Q_{chu} = 3[RE \times (1/ka+1/(ka)^3)]$, where RE is the radiation efficiency of the ESA [8], [9]. Consequently, magnetic-based ESAs usually exhibit a much narrower impedance bandwidth as compared with electric ones [10]-[12].

Many effective methods have been adopted to expand the operational bandwidths of magnetic ESAs to promote their potential applications in wideband space-limited platforms. They can be generally classified into the two categories: passive and active solutions. For example, multiple passive magnetic-based NFRP elements have been employed to attain several overlapping resonances [13]-[15]. The integration of active elements, e.g., non-Foster circuits [16] and varactor diodes [17], [18] into the NFRP radiators have led to significantly enhanced instantaneous operational bandwidths, but at the cost of DC power sources and complex circuits being required.

On the other hand, recently reported metasurface antennas (MSAs) [19]-[25] have interesting low profile and wide bandwidth merits. By exciting a discrete sub-wavelength patch array with either slot-aperture [19]-[21], probe [22],[23] or dipole strip [24],[25], feed structures, multiple resonant modes of the patch array, e.g., the TM_{10} and anti-phase TM_{20} modes [20], were driven and combined to realize a wide operational bandwidth with stable radiation patterns. This technique was utilized recently to realize a simple and effective electric ESA redesign whose prototype exhibited a measured 2.5 times-enhanced bandwidth when compared to its original version [25].

In this Communication, compact, highly efficient linearly polarized (LP) and circularly polarized (CP) magnetic antennas based on interdigitated capacitor-integrated NFRP elements with significantly improved bandwidths are developed. This approach is entirely different from the introduction of multiple passive NFRP elements [13]-[15] or active DC-powered circuits [16]-[18]. As discussed in Section II, the original "intact" capacitively-loaded loop (CLL) NFRP element can be electrically coupled to a driven monopole to excite and efficiently radiate a fundamental magnetic dipole mode [3], [4]. The evolution of the CLL element into an interdigitated capacitor (IDC) version is described. It is explained how the resonance frequency of the first higher order mode of the IDC-based CLL can be controlled by its design. By overlapping it with the fundamental mode, the IDC-based CLL thus provides a much wider bandwidth with stable radiation patterns than the intact one. The resonances corresponding to the fundamental and first higher-order modes of these IDC variants combine to yield significantly enhanced operational bandwidths, i.e., over 5 times those of their original designs. Their bandwidth enhancement mechanisms are explained in detail. A monopole-driven, wideband, LP IDC-CLL NFRP antenna is then introduced in Section III. Simulation results for this variant demonstrate that it has a wide 17.4% fractional bandwidth – a 5 fold enhancement – and a high 95% radiation efficiency and stable radiation patterns over that bandwidth. A monopole-driven, wideband, CP IDC-CLL NFRP antenna is introduced next in Section IV. Its CP performance is achieved by introducing two orthogonal IDC-CLL NFRP elements driven by two electric monopoles fed with a simple coax-based structure. The measured prototype exhibits a wide enhanced CP bandwidth, 8.6% − a 5 fold enhancement – and a high 88% radiation efficiency and uniform radiation patterns over that bandwidth. A summary of the results is given in Section V.

Manuscript received on September 28, 2020; revised on January 7, 2021; and accepted on January 21, 2021.

This work was supported in part by the National Natural Science Foundation of China under Contracts 62001065 and 62061006, in part by the Graduate Scientific Research and Innovation Foundation of Chongqing, China under Contract CYB20066, in part by the Chongqing Natural Science Foundation under Contract cstc2019jcyjjqX0004, and in part by the Australian Research Council under Grant DP160102219. (*Corresponding author: Ming-Chun Tang.*)

X. Chen, M.-C. Tang, and D. Yi are with the Key Laboratory of Dependable Service Computing in Cyber Physical Society Ministry of Education, College of Communication Engineering, Chongqing University, Chongqing 400044, China (E-mail: tangmingchun@cqu.edu.cn).

R. W. Ziolkowski is with the University of Technology Sydney, Global Big Data Technologies Centre, Ultimo NSW 2007, Australia (E-mail: Richard.Ziolkowski@uts.edu.au)

II. IDC Magnetic-based NFRP ESA

Fig. 1(a) compares the two basic magnetic-based NFRP ESA designs. Ant. I consists of a driven dipole element and an "intact" magnetic NFRP element, i.e., a simple CLL with two gaps along the *y*-direction [26]. The CLL element lies on the top surface of a circular sheet of Rogers Duroid™ 6006 whose dielectric constant is $\varepsilon_r = 6.15$ and loss tangent is $tan\ \delta = 0.0019$; the dipole lies on the bottom surface. This configuration yields an LC resonance arising from the inductances and capacitances of both elements [3]. In contrast, the NFRP element of Ant. II has evolved into an eight-unit IDC version of the CLL structure. The multiple fingers of the interdigitated units enhance the capacitance of the CLL structure. The dimensions and placement of the dipole in the two designs are adjusted to maximize the coupling between it and its respective CLL NFRP elements. The increased capacitance introduced by the IDC structure, together with the increased length of the driven dipole, facilitates the excitation of the first higher order mode of the antenna and lowers the ratio of its resonance frequency to that of the fundamental mode.

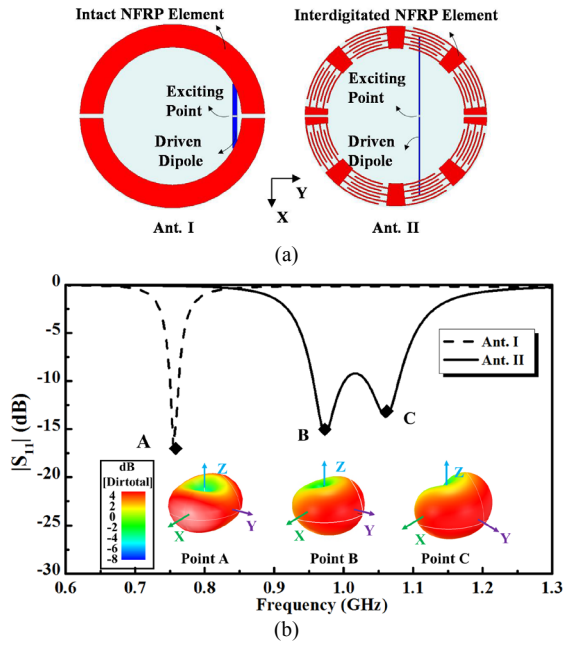

Fig. 1. Two dipole-driven, magnetic-based, NFRP ESAs. (a) Configurations. (b) Simulated $|S_{11}|$ values and the 3-D directivity radiation patterns corresponding to the indicated frequency points.

Fig. 1(b) shows the reflection coefficients ($|S_{11}|$) of the two ESAs. It is readily seen that the fundamental resonant frequency of Ant. I is located at 0.78 GHz. Its –10-dB fractional bandwidth (FBW) is only 1.8%. The corresponding electrical size of the antenna is ka = 0.65. The 3-D directivity pattern is similar to that of a classical magnetic dipole, being nearly omni-directional in the *x0y*-plane. In contrast, Ant. II has two adjacent resonant frequencies, i.e., at 0.97 and 1.06 GHz. They are significantly overlapped to exhibit a wide 9.1% FBW. Although its electrical size witnesses a small increase to ka = 0.80, its impedance bandwidth is over 5 times wider than that of Ant. I. Moreover, even if the electrical size of Ant. I is the same as that of Ant. II, Ant. II still has a ~3 times larger FBW. Note that the 3-D directivity patterns of Ant. II have deep nulls at both resonance frequencies. However, unlike Ant. I, they are essentially unidirectional in both the *x0y*- and *y0z*-planes.

The surface currents density distributions together with the *x0y*-plane cut of the directivity patterns at the resonance frequencies of the two ESAs are depicted and compared in Fig. 2. Fig. 2(a) shows the surface current distributions on the CLL element of Ant. I at 0.78 GHz. The CLL's physical perimeter is 252 mm = 0.65 $\lambda_{0.78\ GHz}$. It is clearly a loop current that is symmetric with respect to the *y*-axis. Consequently, its directivity pattern is as well. However, there is some distortion away from omni because the magnetic dipole is not perfectly formed, i.e., the current density is not uniform. The asymmetric position of the driven dipole causes this outcome.

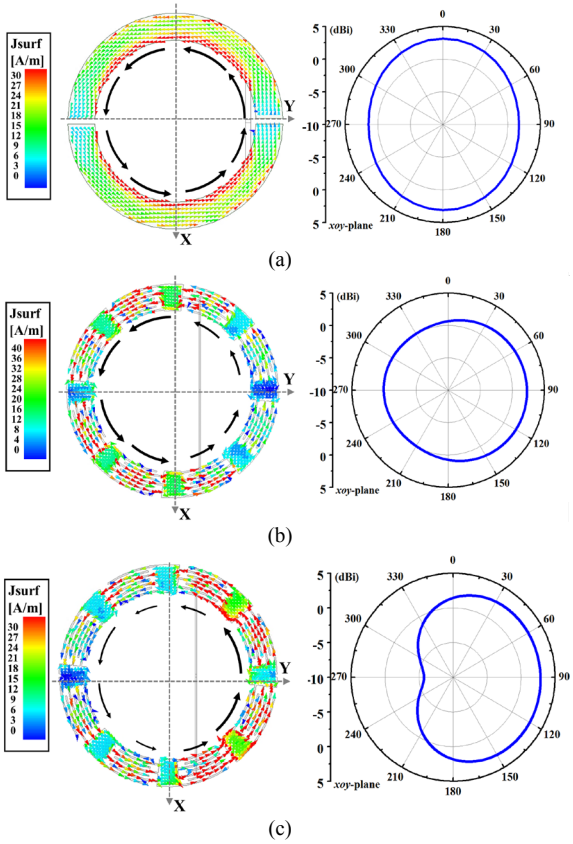

Fig. 2. Surface current distributions on the CLL NFRP elements of the two antennas and the corresponding 2-D directivity patterns in the *x0y*-plane at their resonance frequency points. (a) Ant. I, Point A, 0.78 GHz. (b) Ant. II, Point B, 0.97 GHz. (c) Ant. II, Point C, 1.06 GHz.

Figs. 2(b) and (c) show the surface current distributions on the IDC CLL element of Ant. II at its two resonance frequencies and the resulting 2-D radiation pattern in the *x0y*-plane. The currents on the periodic IDC CLL geometry in Fig. 2(b) are less symmetric with respect to the *x*-axis at the lower frequency, 0.97 GHz, than they are on the simple CLL of Ant. I. Nevertheless, they too are associated with its fundamental mode. Viewing the +*y* half of the IDC CLL as an electric dipole and the back, -*y* half, as one with the opposite current direction, the entire antenna is quasi-Yagi [27], i.e., the front half acts as a director and the back half acts as a reflector in the presence of the driven dipole. Thus the greater directivity in the forward, broadside direction versus the backward one is understood. The front-to-back ratio (FTBR) value is 2.2 dB in the *x0y*-plane.

The surface currents shown in Fig. 2(c) on the IDC CLL element at the higher resonance frequency, 1.06 GHz, resemble the anti-phase first higher order mode of the MSAs in [19]-[24]. It is also interesting to notice that the surface currents are concentrated more on the +*y* side of the CLL with higher amplitudes than on its -*y* side. Thus, the fields radiated by the director of this quasi-Yagi configuration are stronger than those at the lower resonance frequency. This behavior yields a larger FTBR value, 8.5 dB.

In summary, the dipole-driven magnetic-based IDC-CLL NFRP ESA exhibited a 5-fold enhancement of the –10-dB impedance bandwidth when compared to the original, simple, intact CLL version. This enhanced bandwidth performance encouraged us to redesign previously developed monopole-driven magnetic-based NFRP antennas [3] with this IDC-CLL innovation.

III. Wideband, Monopole-Driven, LP Antenna Design

The monopole-driven, LP antenna with its innovative IDC-CLL NFRP element is shown in Fig. 3(a). In contrast to Ant. II in Fig. 1, the magnetic NFRP element is divided in half and is oriented perpendicular to and in the center of a large circular metal ground [13]-[18]. The metal ground serves two functions. On the one hand, it preserves the "loop current" characteristics of the fundamental and adjacent first higher-order modes of the IDC-CLL NFRP element shown in Figs. 2(b) and 2(c) because of the associated image arising from the ground [28]. On the other hand, the fields generated by the currents on the ground cancel much of the back radiated fields. This leads to most of the radiated power being directed into the upper hemisphere rather than into both hemispheres as a figure-8 pattern with its null along the *x*-direction. The optimized design parameters are given in Table I. As shown in Fig. 3(b), the rectangular monopole-driven strip is etched on one side of a semi-circular disk of the 6006 substrate. The driven strip is offset away from the center of the ground and is excited with the center conductor of a 50-Ω source coax fed through a tiny hole in it. The IDC-CLL NFRP element contains 8 IDC units. Each IDC unit has 10 fingers and the length of the fingers is quantified by the angle θ_2 = 15.5°. The length of the connection strips between the full units is separated by the indicated angle θ_1 = 7.0°. Those at the two ends of the CLL are quantified by half that angle, $\theta_1/2$ = 3.5°. The gap between fingers and the connection strips is quantified by the angle θ_3 = 0.5°. The width of each finger is W_1 = 0.5 mm with a gap of g_1 = 0.5 mm between each finger.

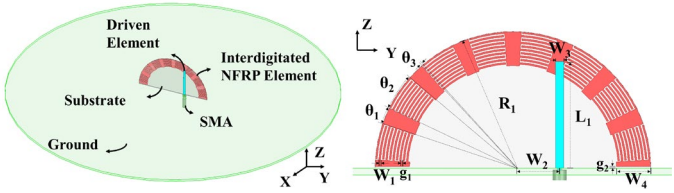

(a) (b)

Fig. 3. The LP monopole-driven IDC-based NFRP antenna configuration. (a) 3-D isometric view. (b) Side view in the *y0z* plane.

The optimized monopole-driven, LP antenna was fabricated, assembled, and measured. The assembled prototype is shown in Fig. 4. The $|S_{11}|$ was measured with an Agilent E8361A PNA Vector Network Analyzer. The far-field radiation performance of the antenna was measured using an SG128 multi-probe antenna measurement system at the China Academy of Information and Communications Technology, Chongqing, China [29]. The measured and simulated $|S_{11}|$ values together with realized gain values are presented in Fig. 4. It indicates that the antenna exhibits a wide measured (simulated) –10-dB bandwidth from 1.10 - 1.31 GHz (1.12 - 1.30 GHz), corresponding to a 17.4% (14.9%) FBW, which is much wider than the corresponding one with its simple, intact CLL NFRP element (~2.9%) [17]. There are clearly two resonant frequency points; they are located at 1.15 and 1.25 GHz (1.15 and 1.27 GHz), respectively. The total electric size of the magnetic NFRP element, which is the main radiator of the antenna, is ka = 0.921, corresponding to the lower frequency bound of the operational bandwidth. The measured (simulated) boresight realized gain values are maintained near 5.5 dBi (6.7 dBi) across the operational band. The simulated RE values are higher than 95% over the entire band. The measured results witnessed a small 20 MHz red-shift, i.e., 1.7%, from the simulated ones which have been confirmed numerically to have resulted from minor errors originating from the fabrication, installation, and measurement processes. Moreover, the driven strip does not act as a monopole radiator in the operating band. Because of its size, its resonance frequency is located at a much higher frequency (1.8GHz). Consequently, it does not perturb the radiation performance of the antenna in its operating band.

Table I. Optimized Design Parameters of the LP Prototype

g_1 = 0.5mm	g_2 = 0.5mm	L_1 = 31.2mm	W_1 = 0.5mm
W_2 = 13.5mm	W_3 = 0.6mm	W_4 = 10mm	R_1 = 40mm
θ_1 = 7deg	θ_2 = 15.5deg	θ_3 = 0.5deg	NULL

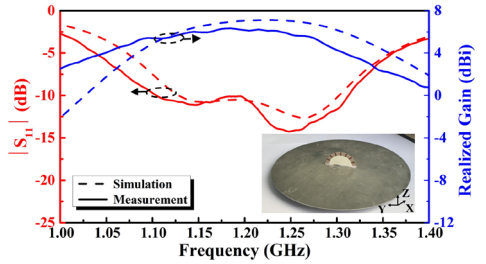

Fig. 4. Measured and simulated $|S_{11}|$ and realized gain values of the LP prototype.

.

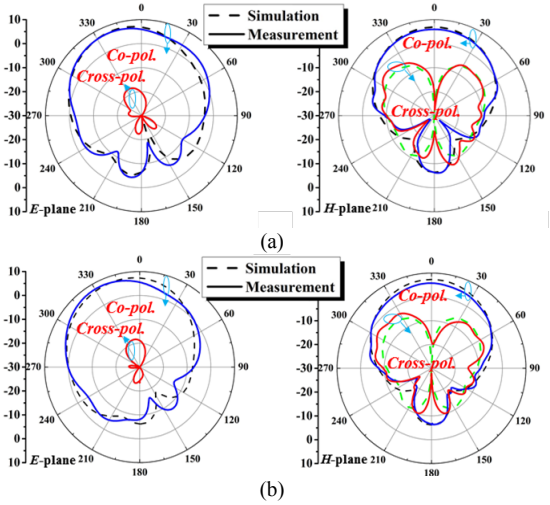

(a)

(b)

Fig. 5. Measured (simulated) realized gain patterns of the LP monopole-driven IDC-based NFRP antenna prototype. (a) Lower resonance frequency, 1.15 (1.15) GHz. (b) Higher resonance frequency, 1.25 (1.27) GHz.

Fig. 5 presents the realized gain patterns at the two resonance frequencies. The LP antenna produces broadside radiation patterns that are stable and uniform over the entire operational band. They are quite different from those emitted by a standard monopole-like radiator which has a deep null along its axis [28]. Moreover, their peak values are considerably larger as well. Because the NFRP element radiates as an effective magnetic dipole that is parallel to the ground plane, its image facilitates this increase. Fig. 6 displays the current distributions on the IDC-CLL NFRP element at its two resonance frequencies. The fundamental "loop current" and the first-higher-mode anti-phase "equivalent loop current" distributions are clearly observed. They produce the realized patterns noted to be uniform over the entire operational bandwidth. These current distributions have behaviors similar to those shown in Figs. 2(b) and (c). The surface currents at the lower resonance frequency are concentrated mostly around the middle sections of the IDC-CLL NFRP element and resemble the fundamental "loop current" mode in

Fig. 2(b). The surface current distribution on the IDC-CLL NFRP element at the higher resonance frequency is concentrated primarily on the *+y* near-vertical side, near the monopole. The currents thus resemble those associated with the anti-phase first higher-order mode shown in Fig. 2(c). This concentration produces the slight tilt of the *E*-plane realized gain patterns in Fig. 6(b). Parameter studies have demonstrated that most of surface currents on the ground plane are concentrated near the NFRP element. Consequently, they have minimal impact on the $|S_{11}|$ and realized gain values if the ground plane radius is larger than the selected value, 60.0 mm.

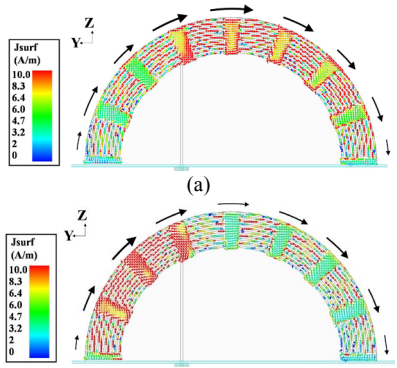

Fig. 6. Simulated current distributions on the LP monopole-driven IDC-based NFRP antenna prototype looking from the *–x* direction. (a) 1.15 GHz. (b) 1.27 GHz.

Studies helped understand the impact of key design parameters on the LP antenna's performance characteristics. For example, the effect of changing the gap size between the IDC NFRP element and the ground is shown in Fig. 7. When the arc angle of the gap, θ_4, decreases, the higher resonance witnesses a red-shift while the lower one remains relatively unchanged. Basically, the gap affects the capacitive couplings in the entire IDC structure. It thus adjusts the frequency ratio between the first higher order mode and the fundamental mode.

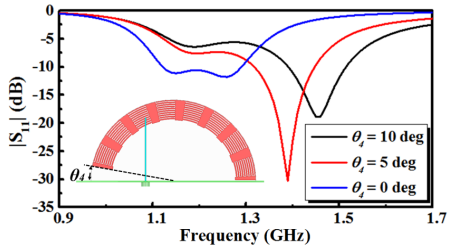

Fig. 7. The effect of the arc angle of the gap, θ_4, between the IDC NFRP element and the ground on the LP antenna's impedance match.

The impact of different numbers of the IDC units in the NFRP element on the antennas' performance characteristics was also parametrically studied. Fig. 8 shows the simulated $|S_{11}|$ results, which indicate that the electrical size of the antenna decreases along with the bandwidth when the number of IDC units decreases. Even though its bandwidth is only slightly larger and its match to the source is not as perfect as the intact version, the electrical size of the two IDC-unit antenna is actually a bit smaller. Moreover, the entire antenna – ground plane included – is electrically small with ka = 0.94. Furthermore, while the two resonant modes are excited when the number of IDC units in the NFRP element is smaller than 8, one does not see both because they significantly overlap. It is not until 8 IDC units are present to see their individual match to the source. It is now understandable why the 8 IDC-unit version was selected for the LP prototype – it yielded a good separation of these two modes while maintaining their nice overlap to yield the largest bandwidth of all of the indicated designs.

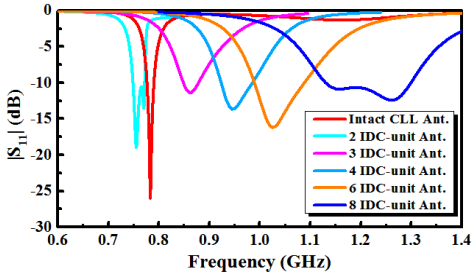

Fig. 8. Simulated $|S_{11}|$ values of the LP design when its NFRP element is constructed with different numbers of IDC units.

Table II provided a comprehensive comparison between the LP prototype and recently reported electrically small magnetic-based antennas, i.e., those with $ka_{radiator}$<1. The size, FBW, RE, Q factor, and Q_{ratio} values are provided. The latter are calculated according to [8], [9] as follows: $Q = 2 / (3 \times \text{FBW}_{-10\text{dB}})$, $Q_{Chu} = (1/ka + 1/(ka)^3)$, $Q_{ratio} = Q / [RE \times 3 \times Q_{\text{Chu}}]$. It is clearly observed that our innovative design has the largest FBW and lowest Q and Q_{ratio} values, which verifies its efficacy and re-enforces its distinct advantage in improving the bandwidth of magnetic antennas with compact size.

TABLE II. COMPARISON BETWEEN THE DEVELOPED IDC-CLL BASED LP ANTENNA AND RECENTLY REPORTED MAGNETIC-BASED ANTENNAS

Refs.	Electrical Size of Radiator ($ka_{radiator}$)	FBW	RE	Q Factor	Q_{ratio}
[14]	0.90	6.13%	80%	11.1	2.97
[30]	< 0.26	-	73%	564.0	3.41
[31]	0.41	1.8%	81%	37.03	1.8
[32]	0.804	5.4%	85%	12.34	1.52
[33]	0.21	2.33% ($\text{FBW}_{-3\text{dB}}$)	11%	85.6	2.31
[34]	0.85	2.5%	56%	26.7	5.67
Reported LP antenna	0.921	17.4%	95%	3.83	0.59

IV. WIDEBAND, MONOPOLE-DRIVEN, CP ANTENNA DESIGN

The IDC design concept was also applied to the related monopole-driven, CP antenna design to expand its operational CP bandwidth. Fig. 9(a) is an isometric view of the configuration of this CP antenna; the corresponding optimized design parameters are given in Table III. In contrast to the LP design, the CP antenna consists of two orthogonal, vertically oriented IDC-CLL NFRP elements printed on two half-disks of the same 6006 substrates and combined in an intersecting wine box-spacer configuration. Two printed monopoles, one for each NFRP element, are driven with a simple coax-driven feed structure [3], [18]. The feed structure is orthogonal and symmetrical with respect to the f = 45° plane as illustrated in Fig. 9(b). Figs. 9(c) and 9(d) show that each IDC-CLL NFRP element is the same as in the LP design in Fig. 3. Note that the offset of the coax cable feed point away from the midpoint of the feeding structure, i.e., changing L_3 in Fig. 9(b), is an effective way to optimize the impedance match while maintaining good CP radiation performance characteristics, especially in the higher portion of the frequency band.

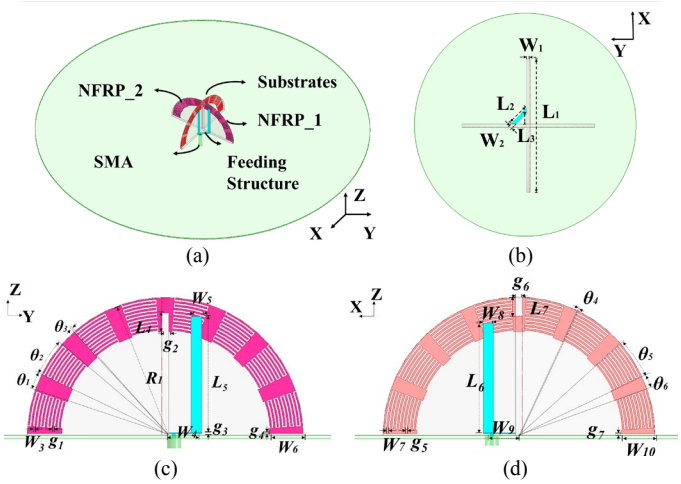

Fig. 9. The geometry of the CP monopole-driven IDC-based NFRP antenna. (a) 3D isometric view. (b) Top view. (c) Side view of the *y0z*-plane cut. (d) Side view of the *z0x*-plane cut.

The optimized CP antenna was also fabricated, assembled and tested. Photos of the assembled prototype are indicated in Figs. 10(a). In Fig. 10(a), the measured (simulated) results indicate that the antenna exhibits a wide –10-dB impedance bandwidth from 1.09 - 1.26 GHz (1.08 - 1.24 GHz), corresponding to a fractional bandwidth of 14.4% (13.8%). The realized gain values are quite stable ~5.2 dBi (~6.5 dBi) and the simulated *RE* values are greater than 88% over the entire operational bandwidth.

TABLE III. OPTIMIZED DESIGN PARAMETERS OF THE CP PROTOTYPE

$g_1 = 0.56mm$	$g_2 = 2mm$	$g_3 = 0.5mm$	$g_4 = 0.5mm$
$g_5 = 0.54mm$	$g_6 = 2mm$	$g_7 = 0.5mm$	$L_1 = 80mm$
$L_2 = 12.2mm$	$L_3 = 5.6mm$	$L_4 = 5.5mm$	$L_5 = 34.4mm$
$L_6 = 32.4mm$	$L_7 = 5.5mm$	$R_1 = 40mm$	$W_1 = 0.508mm$
$W_2 = 0.28mm$	$W_3 = 0.44mm$	$W_4 = 8.9mm$	$W_5 = 0.25mm$
$W_6 = 10mm$	$W_7 = 0.46mm$	$W_8 = 0.12mm$	$W_9 = 8.9mm$
$W_{10} = 10mm$	$\theta_1 = 5.7deg$	$\theta_2 = 16.8deg$	$\theta_3 = 0.5deg$
$\theta_4 = 0.5deg$	$\theta_5 = 16deg$	$\theta_6 = 6.5deg$	*NULL*

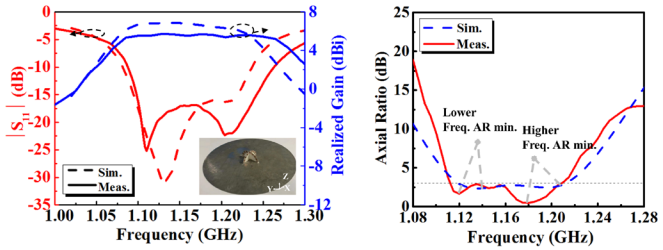

Fig. 10. Measured and simulated results of the CP monopole-driven IDC-based NFRP antenna prototype. (a) $|S_{11}|$ values and realized gain values. (b) AR values.

Fig. 10(b) demonstrates that the associated 3 dB AR bandwidth is from 1.11 to 1.21 GHz (1.12 to 1.215 GHz), corresponding to a fractional bandwidth of 8.6% (8.13%). This bandwidth is substantially wider than the ~1.5% value of the original CLL NFRP CP antenna [18]. The electric size of the NFRP radiating element is ka = 0.923 corresponding to the lower frequency bound of the 3-dB AR bandwidth. Note that the measured resonance frequencies experience about a 10 MHz red-shift which is only 0.8% different from the simulated value. Again, this small difference is attributed to the fabrication, assembly and measurement errors.

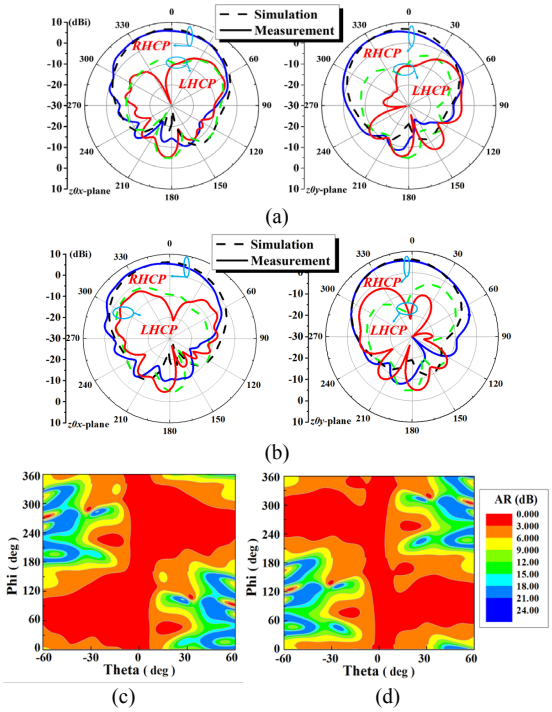

Fig. 11. Radiation performance of the CP antenna at its lower AR minimum, 1.12 (1.13) GHz, and its higher AR minimum, 1.18 (1.2) GHz. Realized gain patterns, (a) and (b), and measured AR over their corresponding beamwidths, (c) and (d).

Fig. 11 presents the measured (simulated) radiation performance at the two frequencies at which the AR values are minimal, 1.12 GHz (1.13 GHz) and 1.18 GHz (1.2 GHz). Fig. 12 displays the current distributions on the two IDC-CLL NFRP elements at these two frequencies. The surface currents at the lower AR minimum are concentrated around the middle sections of the two NFRP elements. They are analogous to those of the fundamental mode at the lower resonance frequency of the LP antenna shown in Fig. 6(a). Similarly, the surface currents at the higher AR minimum are concentrated along the two near-vertical sides of the NFRP elements. They too are analogous to those of LP antenna in its first higher order mode shown in Fig. 6(b). The CP operation is attained because the surface currents on these two orthogonal NFRP elements have approximately a 90° phase difference at both of the AR-minimum frequencies. Because the *z0x* dipole is longer than the *y0z* one, the IDC-CLL NFRP element in the *z0x* plane leads the one in the *y0z* plane. This right-hand CP (RHCP, co-pol) and the corresponding left hand CP (LHCP, cross-pol) behaviors are shown in Figs. 11(a) and (b) at its lower and upper AR minima, respectively. Figs. 11(c) and (d) display the corresponding AR values at different polar angles. The variations arise from the asymmetrical placement of the driven elements and feed structure with respect to the IDC-CLL NFRP elements.

V. CONCLUSION

The bandwidths of several metamaterial-inspired, NFRP antennas were significantly increased by incorporating the innovative magnetic-based IDC-CLL NFRP elements introduced in this work. The IDC-CLL NFRP element concept was first introduced with an ideal dipole-driven magnetic ESA design. A five-fold impedance bandwidth enhancement was demonstrated. Both LP and CP versions of monopole-driven, IDC-CLL NFRP antennas were designed, fabricated and measured. The measured performance characteristics, in good agreement with their simulated values, demonstrate that the IDC-CLL NFRP elements expanded the fractional impedance

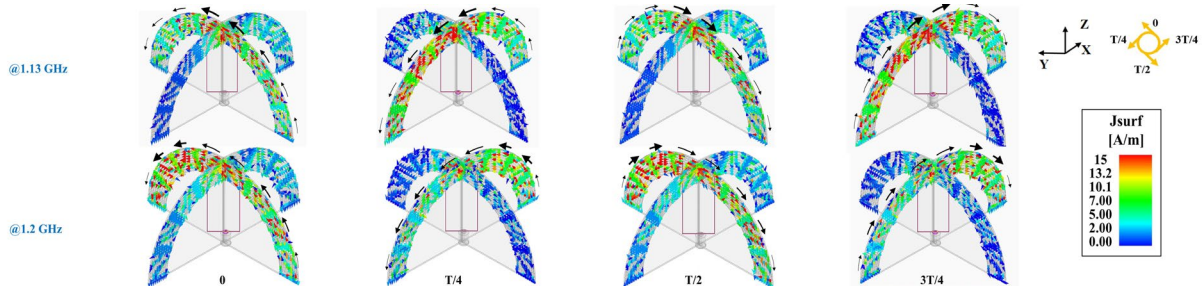

Fig. 12. The surface current distributions on the two IDC-CLL NFRP elements of the monopole-driven CP antenna over one period T = 1 / f_0, where f_0 corresponds to the two frequency points at which the AR dips occur: 1.13 and 1.2 GHz.

bandwidth in the LP case to 17.4%, a 5-fold enhancement in comparison to its original counterpart. Similarly, the fractional AR bandwidth in the CP case was expanded to 8.6%, also a 5-fold enhancement. These magnetic NFRP antenna prototypes have many potential applications in wideband space-limited wireless communication systems that require broad bandwidth LP and CP performance and that exhibit stable realized gain patterns over their entire operating band. Examples include wearable and other compact, portable platforms; indoor base station systems; drones; cubesats; and radio frequency identification systems.

REFERENCES

[1] A. Kurs, A. Karalis, R. Moffatt, J. D. Joannopoulos, P. Fisher, and M. Soljačić, "Wireless power transfer via strongly coupled magnetic resonances," *Science*, vol. 317, no. 5834, pp. 83–86, Jul. 2007.

[2] H. A. Wheeler, "Fundamental limitations of small antennas," *Proc. IRE*, vol. 35, no. 12, pp. 1479-1484, Dec. 1947.

[3] R. W. Ziolkowski, P. Jin, and C.-C. Lin, "Metamaterial-inspired engineering of antennas," *Proc. IEEE*, vol. 99, no. 10, pp. 1720–1731, Oct. 2011.

[4] P. Jin and R. W. Ziolkowski, "Multi-frequency, linear and circular polarized, metamaterial-inspired, near-field resonant parasitic antennas," *IEEE Trans. Antennas Propag.*, vol. 59, no. 5, pp. 1446–1459, May 2011.

[5] S. Kim, Y. Ren, H. Lee, A. Rida, S. Nikolaou, and M. M. Tentzeris, "Monopole antenna with inkjet-printed EBG array on paper substrate for wearable applications," *IEEE Antennas Wireless Propag. Lett.*, vol. 11, pp. 663–666, 2012.

[6] B. Esser, S. R. Beeson, J. C. Dickens, J. J. Mankowski, T. M. Antonsen, and A. A. Neuber, "The path to a transportable ionospheric heater-tuning methods," *IEEE Trans. Plasma Sci.*, vol. 45, no. 6, pp. 1051–1057, Jun. 2017.

[7] N. Zhu, R. W. Ziolkowski, and H. Xin, "Electrically small GPS L1 rectennas," *IEEE Antennas Wireless Propag. Lett.*, vol. 10, pp. 935–938, 2011.

[8] L. J. Chu, "Physical limitations of omni-directional antennas," *J. Appl. Phys.*, vol. 19, pp. 1163–1175, Dec. 1948.

[9] H. L. Thal, "New radiation limits for spherical wire antennas," *IEEE Trans. Antennas Propag.*, vol. 54, no. 10, pp. 2757–2763, Oct. 2006.

[10] A. D. Yaghjian and H. R. Stuart, "Lower bounds on the Q of electrically small dipole antennas," *IEEE Trans. Antennas Propag.*, vol. 58, no. 10, pp. 3114–3121, Oct. 2010.

[11] S. R. Best, "A low Q electrically small magnetic (TE mode) dipole," *IEEE Antennas Wireless Propag. Lett.*, vol. 8, pp. 572–575, 2009.

[12] O. S. Kim and O. Breinbjerg, "Lower bound for the radiation Q of electrically small magnetic dipole antennas with solid magnetodielectric core," *IEEE Trans. Antennas Propag.*, vol. 59, no. 2, pp. 679–681, Feb. 2011.

[13] C.-C. Lin, P. Jin, and R. W. Ziolkowski, "Multi-functional, magnetically-coupled, electrically small, near-field resonant parasitic wire antennas," *IEEE Trans. Antennas Propag.*, vol. 59, no. 3, pp. 714–724, Mar. 2011.

[14] M.-C. Tang, Y. Chen, T. Shi and R. W. Ziolkowski, "Bandwidth-enhanced, compact, near-field resonant parasitic filtennas with sharp out-of-band suppression," *IEEE Antennas Wireless Propag. Lett.*, vol. 17, no. 8, pp. 1483–1487, Aug. 2018.

[15] M.-C. Tang, X. Chen, M. Li, and R. W. Ziolkowski, "Particle swarm optimized, 3-D-printed, wideband, compact hemispherical antenna," *IEEE Antennas Wireless Propag. Lett.*, vol. 17, no. 11, pp. 2031–2035, Nov. 2018.

[16] T. Shi, M.-C. Tang, Z. Wu, H.-X. Xu, and R. W. Ziolkowski, "Improved signal-to-noise ratio, bandwidth-enhanced electrically small antenna augmented with internal non-Foster elements," *IEEE Trans. Antennas Propag.*, vol. 67, no. 4, pp. 2763–2768, Nov. 2019.

[17] M.-C. Tang, and R. W. Ziolkowski, "Frequency-agile, efficient, near-field resonant parasitic monopole antenna," *IEEE Trans. Antennas Propag.*, vol. 62, no. 3, pp. 1479–1483, Mar. 2014.

[18] M.-C. Tang, and R. W. Ziolkowski, "Frequency-agile, efficient, circularly polarized, near-field resonant antenna: designs and measurements," *IEEE Trans. Antennas Propag.*, vol. 63, no. 11, pp. 5203–5209, Nov. 2015.

[19] W. Liu, Z. N. Chen, and X. Qing, "Metamaterial-based low-profile broadband mushroom antenna," *IEEE Trans. Antennas Propag.*, vol. 62, no. 3, pp. 1165–1172, Mar. 2014.

[20] W. Liu, Z. N. Chen, and X. Qing, "Metamaterial-based low-profile broadband aperture-coupled grid-slotted patch antenna," *IEEE Trans. Antennas Propag.*, vol. 63, no. 7, pp. 3325–3329, Jul. 2015.

[21] Z. Wu, X. Chen, and K. Li, "Dual-band antenna integrating with rectangular mushroom-like superstrate for WLAN applications," *IEEE Antennas Wireless Propag. Lett.*, vol. 15, pp. 1269–1272, 2016.

[22] F. H. Lin and Z. N. Chen, "Probe-fed broadband low-profile metasurface antennas using characteristic mode analysis," in *Proc. IEEE Asia–Pacific Conf. Antennas Propag. (APCAP)*, pp. 664–666, Oct. 2017.

[23] W. E. I. Liu, Z. N. Chen, and X. Qing, "Broadband low-profile L-probe fed metasurface antenna with TM leaky wave and TE surface wave resonances," *IEEE Trans. Antennas Propag.*, vol. 68, no. 3, pp. 1348–1355, Mar. 2020.

[24] S. S. S. Nasser, W. Liu, and Z. N. Chen, "Wide bandwidth and enhanced gain of a low-profile dipole antenna achieved by integrated suspended metasurface," *IEEE Trans. Antennas Propag.*, vol. 66, no. 3, pp. 1540–1544, Mar. 2018.

[25] X. Chen, M.-C. Tang, D. Yi, and R. W. Ziolkowski, "Wideband, electrically small, near-field resonant parasitic dipole antenna with stable radiation performance," *IEEE Antennas Wireless Propag. Lett.*, vol. 19, no. 5, pp. 826–830, May 2020.

[26] P. Jin and R. W. Ziolkowski, "Metamaterial-inspired, electrically small Huygens sources," *IEEE Antennas Wireless Propag. Lett.*, vol. 9, pp. 501–505, 2010.

[27] M.-C. Tang, B. Zhou, Y. Duan, X. Chen, and R. W. Ziolkowski, "Pattern-reconfigurable, flexible, wideband, directive, electrically small near-field resonant parasitic antenna," *IEEE Trans. Antennas Propag.*, vol. 66, no. 5, pp. 2271–2280, May 2018.

[28] C. A. Balanis, *Antenna Theory: Analysis and Design*, 3rd. Hoboken, NJ, USA: Wiley Interscience, 2005.

[29] SG128 multi-probe antenna measurement system. [Online]. Available: https://www.mvg-world.com/en/system/files/datasheet_sg128_bd.pdf.

[30] O. S. Kim, ''Low-*Q* electrically small spherical magnetic dipole antennas,'' *IEEE Trans. Antennas Propag.*, vol. 58, no. 7, pp. 2210–2217, Jul. 2010.

[31] J. Kim and S. Nam, ''A compact quasi-isotropic antenna based on folded split-ring resonators,'' *IEEE Antennas Wireless Propag. Lett.*, vol. 16, pp. 294–297, 2017.

[32] K. Wei, Z. Zhang, Z. Feng and M. F. Iskander, ''A MNG-TL loop antenna array with horizontally polarized omnidirectional patterns,'' *IEEE Trans. Antennas Propag.*, vol. 60, no. 6, pp. 2702–2710, Jun. 2012.

[33] K. N. Madsen, Y. Zhou and D. F. Sievenpiper, "A simplified low-*Q* electrically small magnetic dipole antenna," *IEEE Antennas Wireless Propag. Lett.*, vol. 15, pp. 1975–1978, 2016.

[34] P. F. Hu, Y. M. Pan and B. Hu, "Electrically small, planar, complementary antenna with reconfigurable frequency," *IEEE Trans. Antennas Propag.*, vol. 67, no. 8, pp. 5176–5184, Aug. 2019.